

Phenomenological model for first-order elastocaloric materials

Modèle phénoménologique pour les matériaux élastocaloriques de premier ordre

Nora Bachmann^{a,b,*}, Andreas Fitger^a, Sabrina Unmüßig^a, David Bach^a, Olaf Schäfer-Welsen^a, Thomas Koch^b, Kilian Bartholomé^{a,*}

^a Fraunhofer Institute for Physical Measurement Techniques IPM, Thermal Energy Converters, Georges-Köhler-Allee 301, 79110 Freiburg, Germany

^b Karlsruhe Institute of Technology (KIT), Institute of Internal Combustion Engines IFKM, Rintheimer Querallee 2, 76131 Karlsruhe, Germany

ARTICLE INFO

Keywords:

Elastocaloric cooling
Shape memory alloy
Material model
System simulation
Material efficiency

Mots clés:

Refroidissement élastocalorique
Alliage à mémoire de forme
Modélisation de matériau
Simulation de système
Efficacité du matériel

ABSTRACT

Elastocaloric cooling systems may offer a potentially more efficient as well as environmentally friendly alternative to compressor-based cooling technology. These cooling systems use stress-induced phase transformation in elastocaloric materials to pump heat. Thermodynamically consistent material models can be used to design and quantify the efficiency of these cooling systems. In this paper, we present a phenomenological material model that depicts the behavior of first-order materials during stress-induced phase transformation. This model is based on a phenomenological heat capacity equation, from which the parameters adiabatic temperature change and isothermal entropy can be derived. Hysteresis of the materials, which determines its dissipative effects, is also taken into account. Based on this model, these parameters can be calculated as a function of stress and temperature. The performance coefficients derived from the model can be used to evaluate the materials efficiency. Furthermore, the data obtained using this model coincided very closely with experimental data.

Nomenclature

Roman

c_0	specific baseline heat capacity [J kg ⁻¹ K ⁻¹]
c_p	heat capacity [J kg ⁻¹ K ⁻¹]
COP_{Mat}	coefficient of performance for material [-]
FOM	figure of merit [-]
h	specific enthalpy [m ² s ⁻²]
E	Young's-modul [MPa]
q_{diss}	specific dissipative energy [J kg ⁻¹]
S	entropy [J K ⁻¹]
s	specific entropy [J kg ⁻¹ K ⁻¹]
s_{iso}	specific, isothermal entropy change of the caloric material [J kg ⁻¹ K ⁻¹]
T	temperature [K]
T_0	peak temperature of specific heat capacitance with no external field [K]
ΔT_{ad}	adiabatic temperature change [K]
$\Delta T_{ad,rev}$	reversible, adiabatic temperature change [K]

$T_{\sigma_{max}}$	temperature at maximum stress [K]
ΔT_{hys}	thermal hysteresis [K]
T_{irr}	irreversibility of the adiabatic temperature change [K]
T_s	start temperature for integration [K]
W	weighting factor [-]
X	phase composition [-]
Greek letters	
α	model parameter corresponding to the peak width [K]
β	model parameter corresponding to the shift of the peak per applied field [K MPa ⁻¹]
σ	stress [MPa]
δ	error
ε	strain [-]
ρ	density [kg m ⁻³]
Subscripts	
a	austenite
elastic	elastic part of the strain
loading	loading of the elastocaloric material
m	martensite

* Corresponding authors.

E-mail addresses: nora.bachmann@ipm.fraunhofer.de (N. Bachmann), kilian.bartholome@ipm.fraunhofer.de (K. Bartholomé).

<https://doi.org/10.1016/j.ijrefrig.2022.01.009>

Received 2 August 2021; Received in revised form 12 January 2022; Accepted 13 January 2022

Available online 15 January 2022

0140-7007/© 2022 The Author(s). Published by Elsevier B.V. This is an open access article under the CC BY license (<http://creativecommons.org/licenses/by/4.0/>).

max	maximal
min	minimal
pseudoelastic	pseudoelastic part of the strain
rev	reversible
unloading	unloading of the elastocaloric material
Acronyms	
DSC	differential scanning calorimetry
Ni	nickel
Ti	titanium

1. Introduction

When it comes to covering the growing demand for cooling technology, elastocaloric cooling technologies may offer an environmentally friendly, and potentially more efficient, alternative to compressor-based cooling technology (Goetzler et al., 2014). At present these elastocaloric cooling systems are based on materials that are already used in medical technology or in actuating elements as shape-memory alloys. A reversible structural transformation from austenite to martensite can be induced in these materials by applying a load. During this exothermal process, the material heats up and then releases this heat into its surroundings. Once the load is removed, the material will transform back into its original lattice structure, cooling down to below the ambient temperature and absorbing heat from the surrounding environment. This reversible process is known as an “elastocaloric effect” (Kitanovski et al., 2015), with adiabatic temperature changes of up to 25 K possible (Chen et al., 2019). By repeating this process cyclically, heat can be pumped from a cold to a hot reservoir. Initial prototypes of these kinds of elastocaloric cooling systems have already been developed (Bruederlin et al., 2019; Kirsch et al., 2018; Snodgrass and Erickson, 2019; Tušek et al., 2015). For simulation-based system optimization and prediction of the efficiency, thermodynamically consistent material models are required which are based on fundamental equations of thermodynamics.

In this paper, we present a material model that can be used to calculate adiabatic temperature changes, isothermal entropy change and material strain. This model also takes into account hysteresis losses occurring during the transformation process. On this basis conclusions regarding the efficiency of the materials can be drawn. The results of this model were compared with experimental data to confirm its validity.

2. The theory behind elastocaloric phase transitions

Phase transitions in caloric materials can be categorized into first- and second-order type (Smith et al., 2012). For elastocalorics, first-order materials tend to be used since these undergo greater entropy and temperature changes during the phase transition. In the case of first-order materials, the heat capacity peak shifts to higher temperatures when mechanical stress σ is applied (Hess et al., 2020). This shift in the transformation temperature is represented by $\sigma\beta$, where β corresponds to the multiplicative inverse of the Clausius–Clapeyron coefficient. The shape of the curve resulting from this shift remains virtually identical, however.

First-order transformation in elastocaloric materials is usually associated with a hysteretic behavior (Masche et al., 2020). Because of this hysteresis, the material heats up irreversibly during the transformation. At the same time, hysteresis causes the heat capacity temperature peak to shift symmetrically by $\pm \frac{\Delta T_{\text{hys}}}{2}$ during the transformation (c_{a-m}) and reverse transformation (c_{m-a}), as shown in Fig. 1.

3. Material models from literature

Initial models on the behavior of this phase transition describe stress σ as a function of strain ϵ , temperature T , the fraction of martensite and

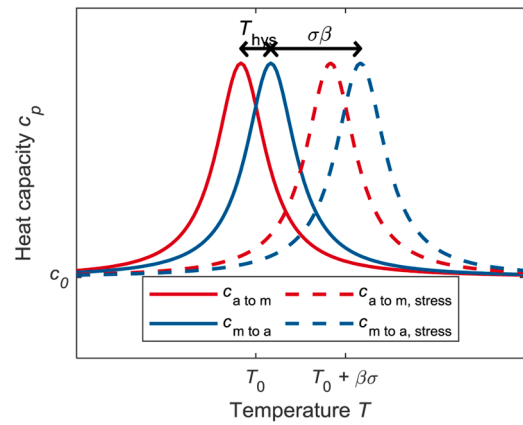


Fig. 1. Shift in the heat capacity peak temperature as a result of applied stress and hysteresis: the dashed lines show the shift to a higher temperature caused by the stress applied, while the shift due to hysteresis is represented by the solid lines. The heat capacity during the phase transformation from austenite (a) to martensite (m) is shown in red (c_{a-m}), while the reverse transformation (c_{m-a}) is shown in blue.

Young’s moduli and apply to both the elastocaloric effect and the shape memory effect (Brinson and Huang, 1996; Lagoudas, 2008; Liang and Rogers, 1990; Tanaka et al., 1995; Tanaka, 1986).

Many models for elastocaloric materials are based on Maxwell’s relations (Bonnot et al., 2008; Gràcia-Condal et al., 2018; Pataky et al., 2015; Tušek et al., 2016; Xiao et al., 2013) and use entropy change δS to calculate the adiabatic temperature change.

$$-\left(\frac{\delta S}{\delta \epsilon}\right)_T = \left(\frac{\delta \sigma}{\delta T}\right)_\epsilon \tag{1}$$

$$\left(\frac{\delta S}{\delta \sigma}\right)_T = \left(\frac{\delta \epsilon}{\delta T}\right)_\sigma \tag{2}$$

To identify the output values for Maxwell’s relations (Eq. (1) and Eq. (2)), strain measurements need to be carried out with different mechanical loads (stresses) (Chen et al., 2019; Gràcia-Condal et al., 2018; Pataky et al., 2015; Xiao et al., 2013) or by varying the material temperature (Chen et al., 2019). Bonnot et al. (2008) and Tušek et al., (2016) also established equations pertaining to strain, enabling the adiabatic temperature change to be specified as a function of stress and temperature. Furthermore, the isothermal entropy change can also be determined using the heat capacity from DSC (differential scanning calorimetry) measurements (Pataky et al., 2015) or by measuring the Clausius–Clapeyron coefficients, i.e. the change in transformation stress with respect to temperature (Chluba et al., 2016; Mañosa et al., 2013).

Models frequently overestimate the adiabatic temperature change (Chen et al., 2019; Pataky et al., 2015; Tušek et al., 2016; Xiao et al., 2013) compared to the measurement. This may be due to less-than-ideal adiabatic measurements in the laboratory or an incomplete phase transformation in the material (Tušek et al., 2016).

In addition, dissipation effects cause an entropy increase during the load cycle (Bonnot et al., 2008). These effects can be attributed to material hysteresis, among other things, and lead to an irreversible temperature change ΔT_{irr} , which can be calculated using stress/strain measurements (Hess et al., 2020; Tušek et al., 2016). Moreover, hysteresis can also be taken into account in a thermodynamically consistent manner by adapting the input parameters for calculating the elastocaloric effect during loading and unloading (Chen et al., 2019; Gràcia-Condal et al., 2018; Pataky et al., 2015; Tušek et al., 2016; Xiao et al., 2013).

Hess et al. (2019) developed a phenomenological model for magnetocalorics. This model describes heat capacity using a Cauchy-Lorentz function based on the temperature and the field applied. This can be used to calculate the adiabatic temperature change ΔT_{ad} and the isothermal entropy change Δs_{iso} .

This model can be expanded to include the thermal hysteresis effect of heat capacity ΔT_{hys} . The resulting dissipative heat q_{diss} corresponds to the enclosed area between the strain curve during loading, $\epsilon_{loading}$, and unloading, $\epsilon_{unloading}$, in the stress-strain graph normalized with the density (Hess et al., 2020).

4. Elastocaloric material model

The model presented in this paper is based on the material model by Hess et al. (2019). This model cannot be applied directly to elastocalorics, however, as the peak of the heat capacity as a function of temperature for elastocaloric materials is much wider than for magnetocaloric materials. The heat capacity equation was therefore adapted to ensure that it is constant when far away from the temperature of the transformation peak. Furthermore, the strain for elastocalorics was calculated based on the field applied using Maxwell's relations (Eq. (2)). This equation consists of an elastic and a pseudoelastic part. The model also reflects incomplete phase transformations. The equations for the model are first specified for a completely reversible phase transformation and then expanded to include the effect of hysteresis.

This model has been adapted for elastocalorics as follows. The heat capacity equation is used to derive the equations for isothermal entropy change Δs_{iso} , adiabatic temperature change ΔT_{ad} , dissipative energy q_{diss} and strain ϵ . These equations can be used to describe loading and unloading with the hysteresis effect. The model will then be compared with the measured values. Material efficiency will also be considered.

4.1. Heat capacity

The heat capacity of an elastocaloric material as a function of temperature T and stress σ can be described using a Cauchy-Lorentz function:

$$c_p(T, \sigma) = \frac{\Delta s_{iso}^{max}}{\pi} \frac{\alpha T}{\alpha^2 + [T - (T_0 + \beta\sigma)]^2} + c_0 \quad (3)$$

This function reaches its peak at temperature T_0 (Fig. 2). Here, c_0 is the heat capacity at a temperature much greater or smaller than the peak temperature (baseline value) and corresponds to the offset of the curve.

$$\begin{aligned} \Delta s_{iso}(T, \sigma) &= s(T, \sigma) - s(T, 0) \\ &= \frac{\Delta s_{iso}^{max}}{\pi} \left\{ \tan^{-1} \left[\frac{T - (T_0 + \beta\sigma)}{\alpha} \right] - \tan^{-1} \left[\frac{T_s - (T_0 + \beta\sigma)}{\alpha} \right] - \tan^{-1} \left(\frac{T - T_0}{\alpha} \right) + \tan^{-1} \left(\frac{T_s - T_0}{\alpha} \right) \right\} \\ &\approx \frac{\Delta s_{iso}^{max}}{\pi} \left\{ \tan^{-1} \left[\frac{T - (T_0 + \beta\sigma)}{\alpha} \right] - \tan^{-1} \left(\frac{T - T_0}{\alpha} \right) \right\} \end{aligned} \quad (5)$$

The half width of the curve is given by α . β is the reciprocal of Clausius–Clapeyron coefficient and determines the shift of the curve when a stress is applied. The area under the curve up to the specific base heat capacity c_0 corresponds to the maximum entropy change Δs_{iso}^{max} , i.e. occurring during a complete transformation from austenite to martensite. On the basis of this stress- and temperature-dependent heat capacity, Maxwell's relations can now be used to analytically calculate

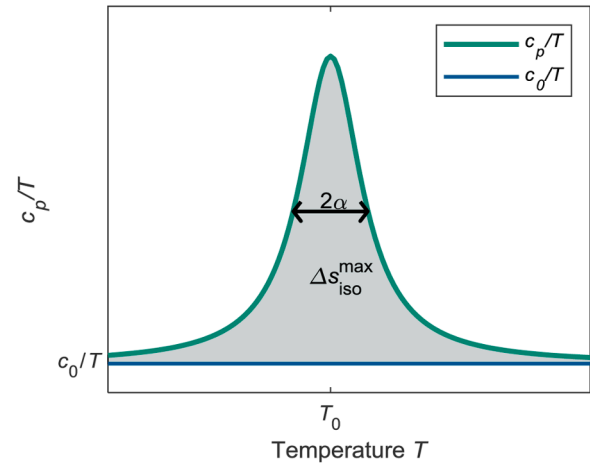


Fig. 2. Heat capacity as a function of temperature: The heat capacity peak is at T_0 and the width of the peak is defined as α . The area under the curve corresponds to the maximum isothermal entropy change during the phase transformation Δs_{iso}^{max} .

the isothermal entropy change Δs_{iso} , adiabatic temperature change ΔT_{ad} , phase composition X and strain ϵ , as shown in the following.

4.2. Isothermal entropy change

The entropy of the elastocaloric material can be calculated by integrating c_p/T from 0 K to temperature T .

$$\begin{aligned} s(T, \sigma) &= \int_{T_s}^T \frac{c_p(T', \sigma)}{T'} dT' \\ &= \frac{\Delta s_{iso}^{max}}{\pi} \tan^{-1} \left[\frac{T - (T_0 + \beta\sigma)}{\alpha} \right] + c_0 \ln(T) \\ &\quad - \frac{\Delta s_{iso}^{max}}{\pi} \tan^{-1} \left[\frac{T_s - (T_0 + \beta\sigma)}{\alpha} \right] - c_0 \ln(T_s) \end{aligned} \quad (4)$$

Here, the auxiliary variable T_s is introduced with $T_s \ll T_0$.

The isothermal entropy change Δs_{iso} describes the entropy change during loading and unloading at a constant temperature T and is represented by:

The approximation applies for $T_s \ll T_0$.

4.3. Adiabatic temperature change

Entropy during a reversible, adiabatic phase transformation is constant. Therefore, entropy will remain the same before and after the application of stress σ to an elastocaloric material with temperature T , i.

e. $s(T, \sigma = 0) = s(T + \Delta T_{ad,rev}, \sigma)$. This results in the following recursive equation for the adiabatic temperature change $\Delta T_{ad,rev}$:

$$\Delta T_{ad,rev}(T, \sigma) = -T + T \exp \left\{ \frac{\Delta s_{iso}^{max}}{c_0 \pi} \left[-\tan^{-1} \left(\frac{T_0 - T}{\alpha} \right) + \tan^{-1} \left(\frac{T_0 - T_s}{\alpha} \right) - \tan^{-1} \left(\frac{T_0 + \beta \sigma - T_s}{\alpha} \right) + \tan^{-1} \left(\frac{T_0 + \beta \sigma - T - \Delta T_{ad,rev}(T, \sigma)}{\alpha} \right) \right] \right\} \quad (6)$$

4.4. Phase composition and Young's modulus

The phase composition during the structural transformation is calculated from the maximum entropy change using the proportion of isothermal entropy change (Fig. 3). The ratio of the area A_X and maximal entropy change Δs_{iso}^{max} is the austenite fraction X and is given by:

$$X(T, \sigma) = \frac{A_X}{\Delta s_{iso}^{max}} = \int_{T_s}^T \frac{c_p(T', \sigma) - c_0}{T' \Delta s_{iso}^{max}} dT' = \frac{1}{\pi} \int_{T_s}^T \frac{\alpha}{\alpha^2 + [T - (T_0 + \beta \sigma)]^2} dT' \\ = \frac{1}{\pi} \left[-\tan^{-1} \left(\frac{\beta \sigma + T_0 - T}{\alpha} \right) + \tan^{-1} \left(\frac{\beta \sigma + T_0 - T_s}{\alpha} \right) \right] \\ \approx \frac{1}{\pi} \left[\tan^{-1} \left(\frac{\beta \sigma + T_0 - T}{\alpha} \right) \right] + \frac{1}{2} \quad (7)$$

$$\varepsilon_{pseudoelastic}(T, \sigma) = \rho \int_{T_s}^T \left(\frac{\delta s}{\delta \sigma} \right)_T dT' \\ = \frac{\Delta s_{iso}^{max} \beta \rho}{\pi} \int_{T_s}^T \left\{ -\frac{\alpha}{\alpha^2 + [T' - (T_0 + \beta \sigma)]^2} + \frac{\alpha}{\alpha^2 + [T_s - (T_0 + \beta \sigma)]^2} \right\} dT' \\ = -\frac{\Delta s_{iso}^{max} \beta \rho}{\pi} \left\{ \tan^{-1} \left[\frac{T - (T_0 + \beta \sigma)}{\alpha} \right] - \tan^{-1} \left[\frac{T_s - (T_0 + \beta \sigma)}{\alpha} \right] \right. \\ \left. - \left[\frac{\alpha T}{\alpha^2 + (T_s - T_0 - \beta \sigma)^2} \right] + \left[\frac{\alpha T_s}{\alpha^2 + (T_s - T_0 - \beta \sigma)^2} \right] \right\} \\ \approx -\frac{\Delta s_{iso}^{max} \beta \rho}{\pi} \left\{ \tan^{-1} \left[\frac{T - (T_0 + \beta \sigma)}{\alpha} \right] - \frac{\pi}{2} - \left[\frac{\alpha T}{\alpha^2 + (T_0 + \beta \sigma)^2} \right] \right\} \quad (10)$$

The approximation applies for $T_s \ll T_0$.

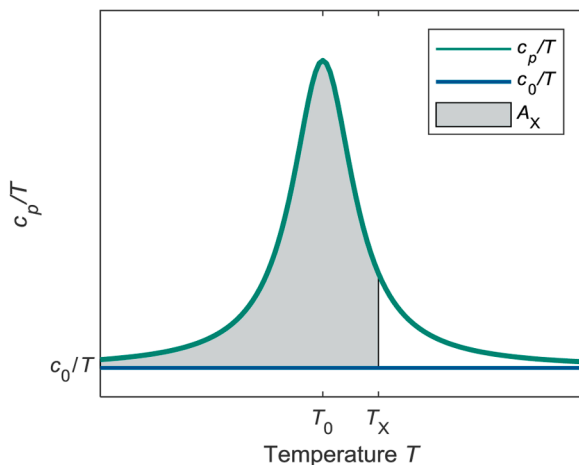


Fig. 3. Phase composition: the phase composition X at temperature T_X is calculated on the basis of the relationship between the area A_X shown in gray and Δs_{iso}^{max} , which corresponds to the area between c_p/T and c_0/T .

With the phase composition, the Young's modulus E can be calculated, which is composed of the Young's moduli of the two phases austenite E_a and martensite E_m :

$$E = E_a X + E_m (1 - X) \quad (8)$$

4.5. Strain

Stress-induced phase transformation results in a strain ε on the material. This is composed of three parts: a pseudoelastic part $\varepsilon_{pseudoelastic}$ due to the structural transformation, an elastic part $\varepsilon_{elastic}$ due to the stress applied and the strain due to the temperature change (Lagoudas, 2008). Since the strain caused by the temperature change in the material is very small, this will not be discussed further here. The strain is adjusted by the offset of the strain without stress, resulting in:

$$\varepsilon(T, \sigma) = \varepsilon_{pseudoelastic}(T, \sigma) - \varepsilon_{pseudoelastic}(T, \sigma = 0) + \varepsilon_{elastic}(T, \sigma) \quad (9)$$

The pseudoelastic part from Eq. (9) can be calculated using Maxwell's relations (Eq. (2)):

ρ is the density of the elastocaloric material. The approximation applies for $T_s \ll T_0$. In addition to the pseudoelastic part, the elastic part also contributes to the strain. This can be calculated using Hooke's law: $\varepsilon_{elastic} = \frac{\sigma}{E}$. This results in the following equation for the strain $\varepsilon(T, \sigma)$:

$$\varepsilon(T, \sigma) = -\frac{\Delta s_{iso}^{max} \beta \rho}{\pi} \left\{ \tan^{-1} \left[\frac{T - (T_0 + \beta \sigma)}{\alpha} \right] - \tan^{-1} \left[\frac{T_s - (T_0 + \beta \sigma)}{\alpha} \right] - \left[\frac{\alpha T}{\alpha^2 + (T_s - T_0 - \beta \sigma)^2} \right] \right. \\ \left. + \left[\frac{\alpha T_s}{\alpha^2 + (T_s - T_0 - \beta \sigma)^2} \right] - \tan^{-1} \left[\frac{T - T_0}{\alpha} \right] \right. \\ \left. + \tan^{-1} \left[\frac{T_s - T_0}{\alpha} \right] + \left[\frac{\alpha T}{\alpha^2 + (T_s - T_0)^2} \right] \right. \\ \left. - \left[\frac{\alpha T_s}{\alpha^2 + (T_s - T_0)^2} \right] \right\} + \frac{\sigma}{E} \quad (11)$$

4.6. Expansion of the model to include dissipative losses

To integrate the hysteresis process into the model, the shift from the heat capacity curve (by $\pm \frac{\Delta T_{hys}}{2}$) is taken into account and the strain equations (Eq. (11)) adapted. Stress-dependent hysteresis, which

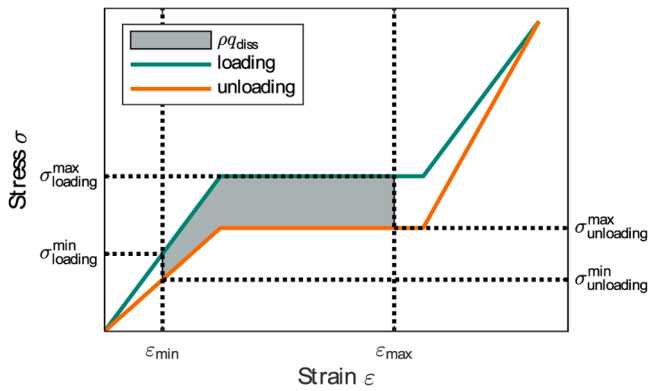


Fig. 4. The dissipative energy for an incomplete transformation of ϵ_{\min} and ϵ_{\max} is proportional to the gray area.

corresponds to the dissipative energy q_{diss} , can be calculated on the basis of this. In the stress-strain graph q_{diss} corresponds to the enclosed area divided by the density ρ :

If the transformation is incomplete, the branches between loading

$$\begin{aligned}
 q_{\text{diss}}(T, \sigma_{\text{loading}}^{\min}, \sigma_{\text{loading}}^{\max}) &= \frac{1}{\rho} \left(\int_{\sigma_{\text{unloading}}^{\min}}^{\sigma_{\text{unloading}}^{\max}} \epsilon_{\text{unloading}}(T, \sigma) d\sigma - \int_{\sigma_{\text{loading}}^{\min}}^{\sigma_{\text{loading}}^{\max}} \epsilon_{\text{loading}}(T, \sigma) d\sigma \right) \\
 &+ \left[\sigma_{\text{loading}}^{\max} \epsilon_{\text{loading}}(T, \sigma_{\text{loading}}^{\max}) - \sigma_{\text{unloading}}^{\max} \epsilon_{\text{unloading}}(T, \sigma_{\text{unloading}}^{\max}) \right] \\
 &- \left[\sigma_{\text{loading}}^{\min} \epsilon_{\text{loading}}(T, \sigma_{\text{loading}}^{\min}) - \sigma_{\text{unloading}}^{\min} \epsilon_{\text{unloading}}(T, \sigma_{\text{unloading}}^{\min}) \right] \\
 &= \frac{1}{\rho} \frac{\Delta T_{\text{hys}}}{\beta} [\epsilon(T, \sigma^{\max}) - \epsilon(T, \sigma^{\min})]
 \end{aligned} \tag{12}$$

and unloading are connected vertically at ϵ_{\min} ($\sigma_{\text{loading}}^{\min}$ and $\sigma_{\text{unloading}}^{\min}$) or ϵ_{\max} ($\sigma_{\text{loading}}^{\max}$ and $\sigma_{\text{unloading}}^{\max}$) to calculate the area (Fig. 4).

The irreversible temperature change is proportional to the dissipative energy: $\Delta T_{\text{irr}} = \frac{q_{\text{diss}}}{c_0}$ (Hess et al., 2020). To calculate the adiabatic temperature change with a hysteresis effect ($\Delta T_{\text{ad, loading}}$ and

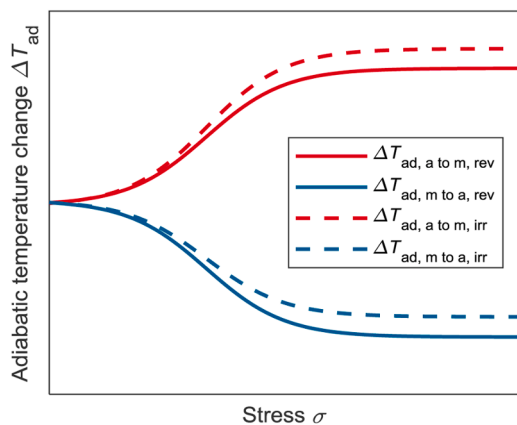


Fig. 5. The reversible adiabatic temperature change is shown using solid lines, while the dashed lines represent the adiabatic temperature change taking into account hysteresis. Red is used to show the temperature change during loading and blue to show the temperature change during unloading.

$\Delta T_{\text{ad, unloading}}$), a distinction is made between loading and unloading:

$$\begin{aligned}
 \Delta T_{\text{ad, loading}} &= \Delta T_{\text{ad, rev}} + \frac{\Delta T_{\text{irr}}}{2} \\
 \Delta T_{\text{ad, unloading}} &= \Delta T_{\text{ad, rev}} - \frac{\Delta T_{\text{irr}}}{2}
 \end{aligned} \tag{13}$$

Fig. 5 shows the adiabatic temperature change with and without a hysteresis effect.

4.7. Material characterization for determining model parameters

To validate the material model, samples of a commercially available alloy from Euroflex GmbH were used, consisting of 56.2% nickel and 43.8% titanium (density of $6,736 \text{ kg m}^{-3}$, austenite finish temperature of $-1.7 \text{ }^\circ\text{C}$) in the form of small tubes (exterior diameter: 2.4 mm, wall thickness: 0.3 mm) and cut to a length of 11 mm. The faces were then polished parallel to the planes.

To determine the heat capacity of the used alloy, a DSC measurement was carried out at Ingpuls GmbH with a heating rate of 10 K min^{-1} . According to the manufacturer's data sheet, the measurement uncertainty is 2% of the measured value. The material was trained for more than 5,000 cycles before the measurement.

For adiabatic and isothermal measurements, three samples were

characterized simultaneously in a test setup. Compressive load was then applied using an eccentric press. The load was measured using a Hottinger Brüel & Kjaer GmbH load cell, while the position was measured using three symmetrically arranged position sensors from eddylab GmbH and the temperature of each sample using type-T thermocouples. The test setup was temperature-controlled.

Before the measurements, the samples underwent 5,000 cycles to train the material at a stress of $895 \text{ MPa} \pm 7 \text{ MPa}$ had established. The preload, maximum strain and strain rate were adjusted. Other parameters result from these settings.

After training the samples, isothermal measurements were carried out with a strain rate of $5 \cdot 10^{-5} \text{ s}^{-1}$ at temperatures of $10 \text{ }^\circ\text{C}$, $20 \text{ }^\circ\text{C}$, $30 \text{ }^\circ\text{C}$ and $40 \text{ }^\circ\text{C}$. The dissipative energy was calculated from the stress-strain data of these measurements using a closed-loop integral of the applied force and the change of length of the ECM divided by the mass.

Adiabatic measurements were performed with a strain rate of 0.1 s^{-1} and a holding time between loading and unloading of 120 s for the same temperatures as the isothermal measurements.

The isothermal and adiabatic stress-strain curves at $20 \text{ }^\circ\text{C}$ at maximum strain are shown in Fig. 6.

For adiabatic measurements, during loading, the maximum temperature $T_{\sigma_{\text{max}}}$ is expected to occur when the maximum stress σ_{max} is applied. Fig. 7 shows the temperature T and stress σ when the material is compressed. The maximum temperature T_{max} was measured with a delay related to the maximum stress σ_{max} . This was due to thermal coupling and the thermal impedance of the thermocouples to the

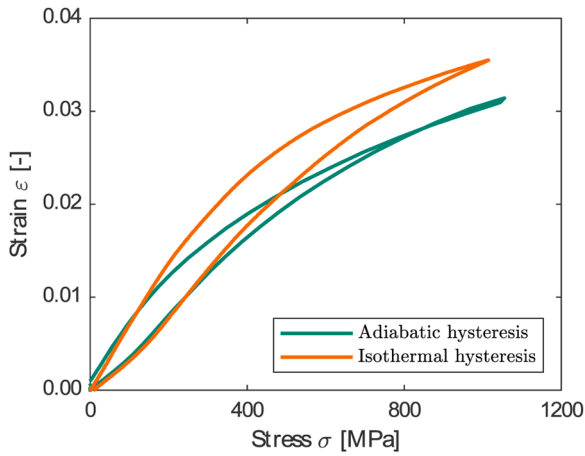


Fig. 6. Adiabatic and isothermal stress-strain curve a temperature of 20 °C.

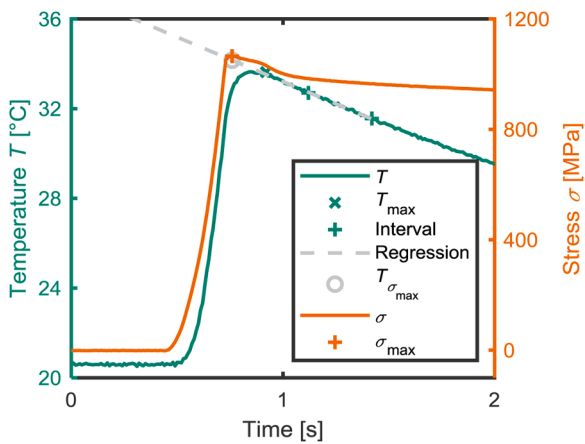


Fig. 7. Stress and temperature profile for an adiabatic measurement during loading. The gray dashed line shows the linear regression of the cooling curve. A maximum temperature change T_{max} is measured. The maximum temperature change is expected to occur when maximum load σ_{max} is applied, however ($T_{\sigma_{max}}$).

elastocaloric material. The data points in the adiabatic measurements were therefore extrapolated from the measured temperature values by means of a linear regression, with the almost linear area of the cooling curve selected as the regression interval. To analyze the errors, a reading of the temperature was taken on the regression line during application of maximum load. The measured values of T_{max} are used in the simulation. The adiabatic temperature change is underestimated, however, as $T_{max} < T_{\sigma_{max}}$ applies. The same applies to the adiabatic temperature change during unloading.

In addition, the measurement uncertainty of the thermocouples of 0.5 K with Gaussian error propagation is taken into account.

The measurement uncertainty of the stress and strain data were calculated using the Gaussian error propagation from the specified measurement uncertainties of the sensor manufacturer. The same applies to the measurement uncertainty of the dissipative energy, which encounters the measurement uncertainty of length change of the material and force.

4.8. Model results and discussion

Heat capacity (Eq. (3)), adiabatic temperature change (Eq. (13)), strain (Eq. (11)) and dissipative losses (Eq. (12)) were simultaneously fitted to the corresponding experimental data by least-square minimization. Each individual value of the input variable is weighted by the

Table 1

Model parameter: After the fit to the input parameters, the model parameters were fitted. 95% of all measured values are found in the interval of deviation from the expected value.

Model parameter	
T_0	$273.90 \text{ K} \pm 0.13 \text{ K}$
ΔT_{hys}	$11.9 \text{ K} \pm 0.6 \text{ K}$
Δs_{iso}^{max}	$42.7 \text{ J kg}^{-1} \text{ K}^{-1} \pm 0.9 \text{ J kg}^{-1} \text{ K}^{-1}$
c_0	$663.6 \text{ J kg}^{-1} \text{ K}^{-1} \pm 1.6 \text{ J kg}^{-1} \text{ K}^{-1}$
α	$26.8 \text{ K} \pm 0.4 \text{ K}$
β	$0.0845 \text{ K MPa}^{-1} \pm 0.0014 \text{ K MPa}^{-1}$
E_a	$56,900 \text{ MPa} \pm 400 \text{ MPa}$
E_m	$42,000 \text{ MPa} \pm 3,000 \text{ MPa}$

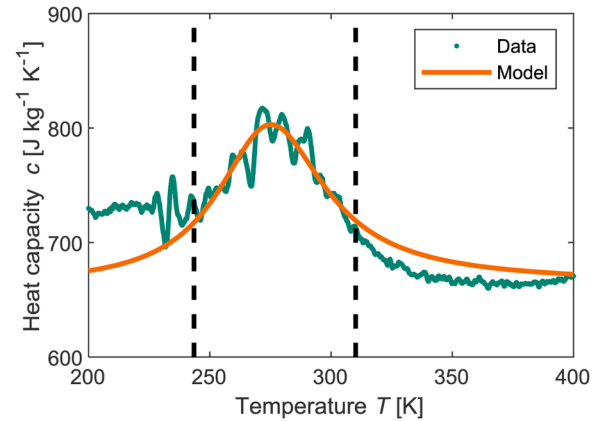


Fig. 8. Measurement data and model for heat capacity. The data between the dashed lines were used for the model.

inverse of the squared error: $W = \frac{1}{\sigma^2}$. This results in the following model parameters with a confidence interval of 95% in Table 1:

Fig. 8 shows measurement data and the results of the model of the heat capacity. Only the data from the relevant temperature range around the peak temperature was used for the model. The adiabatic temperature change that occurred when loading and unloading the material is also represented well by the model (Fig. 9). The curves shift to higher stresses at higher temperatures. The effect of thermal hysteresis can be seen here by the fact that the curves are not symmetrical around 0 K.

For the strain in the isothermal measurement the model is in good agreement with the experimental data (Fig. 10). The trend in the measured values is reflected by the model.

Fig. 11 shows the data of the dissipative energy, which reaches saturation at high stresses, as the transformation is complete in this case. The model underestimates the experimental data at high strains. One reason could be that additional dissipative losses such as friction, which are not caused by the phase transformation and therefore not represented by the model.

The underestimation of dissipative energy at high stresses is also reflected in the adiabatic temperature change curves, since ΔT_{irr} is proportional to dissipative energy.

It has been described in literature, that there can be a discrepancy between a temperature-induced transformation, which is apparent in a DSC measurement, and stress-induced transformation triggered by external forces (Ossmer et al., 2014; Tušek et al., 2016). Here, however, we see that it is possible to represent both heat capacity and adiabatic temperature change data with the model very well, supporting the applicability of this approach.

With this model it is possible to represent the measured values for the heat capacity, the adiabatic temperature change, the strain, and the dissipative energy thermodynamically consistent at the same time and to consider the dissipative effects in the equations. The model was fitted

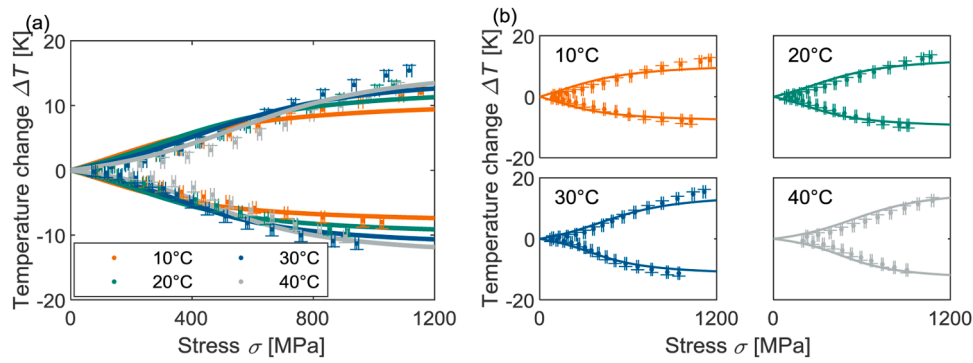


Fig. 9. Measurement data and model showing adiabatic temperature change during loading and unloading. The model is depicted by a solid line. In (a), the data at the four temperatures are shown together to illustrate the temperature effect on the adiabatic temperature change. In (b) the data at the four temperatures are shown individually.

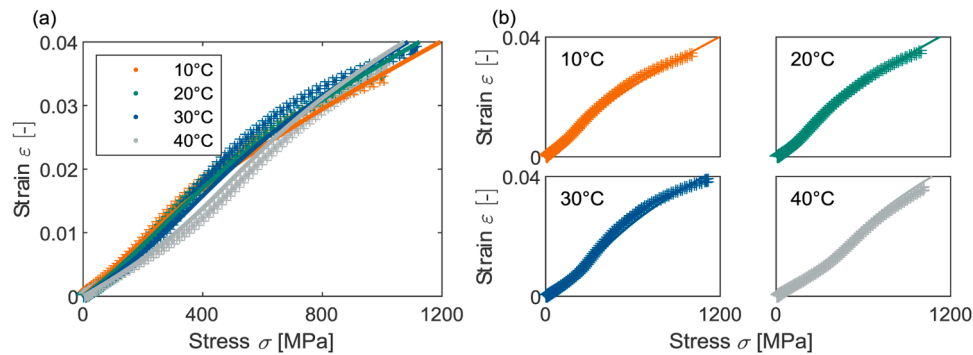


Fig. 10. Measurement data and model for the strain. The model is depicted by a solid line. The four temperatures are shown in one diagram to emphasize the effect of temperature on strain (a). In (b), each plot shows the data at a different temperature.

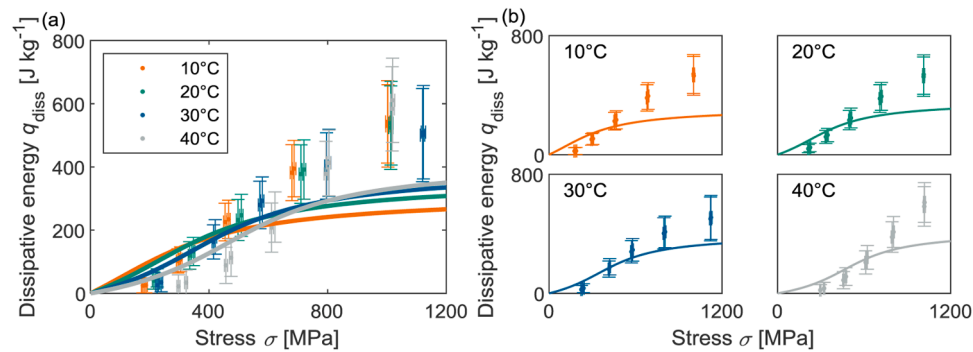


Fig. 11. Measurement data and the model for dissipative heat. The model is depicted by a solid line. In (a) the data at the four temperatures are shown in a diagram and in (b) they are shown individually.

for nickel-titanium alloys, but it is also conceivable to use it for other elastocaloric materials.

4.9. Efficiency

The efficiency with which elastocaloric materials are able to transport heat in a system is primarily determined by the relationship between isothermal entropy change Δs_{iso} and dissipative losses q_{diss} (Hess et al., 2020; Masche et al., 2020; Qian et al., 2016). For a cascaded system, this results in an exergetic efficiency of $\eta \approx \frac{1}{1 + 4 \frac{q_{diss}}{\Delta s_{iso} \Delta T_{ad}}} = \frac{1}{1 + 4 \frac{\Delta T_{hys}}{\Delta T_{ad}}}$ (Hess et al., 2020).

Thus, a figure of merit (*FOM*) as a measure of the material’s quality can be defined by $FOM(T, \sigma) = \frac{\Delta T_{ad}(T, \sigma)}{\Delta T_{hys}}$. The higher this *FOM*, the more efficiently the cascaded system can work. The material parameters calculated here result in the *FOM* dependence on temperature and stress shown in Fig. 12.

In this figure, the higher the stress applied and the temperature, the higher the *FOM*, resulting in an *FOM* value of 1.00 ± 0.06 when the stress is 1,200 MPa and the temperature is 40 °C. Since the dissipative energy is underestimated at high stresses, the *FOM* is overestimated here.

With the maximum *FOM* the maximum possible system efficiency

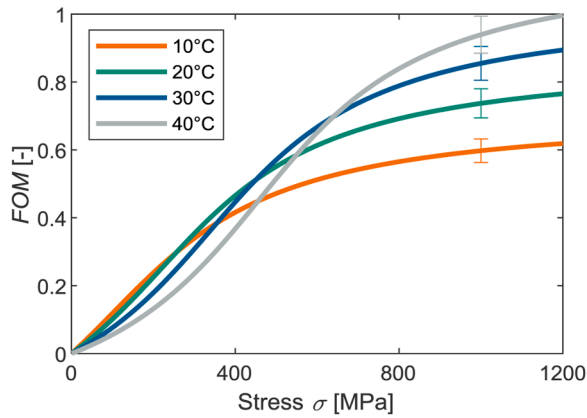


Fig. 12. Figure of merit plotted against stress for four different temperatures. The uncertainty calculated with Gaussian error propagation was entered as an example for a stress of 1000 MPa.

$\eta \approx \frac{1}{1+FOM}$ would be $20.0\% \pm 0.3\%$. This *FOM* should not be confused with COP_{Mat} , which is often used in the literature to describe the performance of a caloric material and is given by the ratio of reversible heat to dissipative losses of the material. COP_{Mat} focuses on the material efficiency and is given by $COP_{Mat} = \frac{c_0 \Delta T_{ad}}{q_{diss}}$ (Tušek et al., 2016), while the *FOM* encounters the thermodynamic efficiency of the material in a cooling cycle. Using the relation $q_{diss} = \Delta s_{iso} \Delta T_{hys}$ (Hess et al., 2020) a relation between COP_{Mat} and *FOM* can be shown: $COP_{Mat} = \frac{c_0 \Delta T_{ad}}{q_{diss}} = \frac{c_0 \Delta T_{ad}}{\Delta s_{iso} \Delta T_{hys}} = \frac{c_0}{\Delta s_{iso}} FOM$.

While *FOM* is increasing with increasing stress (Fig. 12), COP_{Mat} is decreasing (Porenta et al., 2020). This is because of an increase of the isothermal entropy with increasing stress.

To increase this value, materials with lower hysteresis are required, i. e. with smaller values for ΔT_{hys} . System efficiency can also be increased further by using suitable system concepts, such as applying heat regeneration concepts (Qian et al., 2015).

5. Conclusion

Elastocaloric cooling systems are a promising, environmentally friendly alternative to conventional compressor systems. Modeling and simulation play an essential role in developing and optimizing such systems. Material behavior is an important input variable in these system simulations and should therefore be reflected in its entirety. The phenomenological material model presented in this paper expands on the model by Hess et al. (Hess et al., 2020, 2019) for elastocalorics. Adiabatic temperature change, strain, dissipative energy and heat capacity are specified as an equation in relation to temperature and stress; this model coincides very closely with experimental measurement results. Since this modeling approach has already been shown for elastocalorics and magnetocalorics, it is conceivable that it can be applied to electrocalorics as well.

The model can be used for different elastocaloric material alloys in order to calculate performance coefficients regarding the material efficiency. This enables cooling systems to be optimized, which is an important step in the further development of elastocaloric cooling systems.

Declaration of Competing Interest

The authors declare no competing interests.

Acknowledgements

This work was funded by the Federal Ministry of Education and Research (BMBF) of Germany as part of the ElastoCool project (Grant No. 03VP04670).

References

- Bonnot, E., Romero, R., Mañosa, L., Vives, E., Planes, A., 2008. Elastocaloric effect associated with the martensitic transition in shape-memory alloys. *Phys. Rev. Lett.* 100, 125901 <https://doi.org/10.1103/PhysRevLett.100.125901>.
- Brinson, L.C., Huang, M.S., 1996. Simplifications and comparisons of shape memory alloy constitutive models. *J. Intell. Mater. Syst. Struct.* 7, 108–114. <https://doi.org/10.1177/1045389X9600700112>.
- Bruederlin, F., Bumke, L., Quandt, E., Kohl, M., 2019. Cascaded SMA-film based elastocaloric cooling. In: 20th International Conference on Solid-State Sensors, Actuators and Microsystems & Eurosensors XXXIII, pp. 1467–1470. <https://doi.org/10.1109/TRANSDUCERS.2019.8808605>.
- Chen, H., Xiao, F., Liang, X., Li, Z., Li, Z., Jin, X., Fukuda, T., 2019. Giant elastocaloric effect with wide temperature window in an Al-doped nanocrystalline Ti–Ni–Cu shape memory alloy. *Acta Mater.* 177, 169–177. <https://doi.org/10.1016/j.actamat.2019.07.033>.
- Chluba, C., Ossmer, H., Zamponi, C., Kohl, M., Quandt, E., 2016. Ultra-low fatigue quaternary TiNi-based films for elastocaloric cooling. *Shap. Mem. Superelasticity* 2, 95–103. <https://doi.org/10.1007/s40830-016-0054-3>.
- Goetzler, W., Zogg, R., Young, J., Johnson, C., 2014. Energy savings potential and RD&D opportunities for non-vapor-compression HVAC technologies. Navigant Consulting Inc., prepared for US Department of Energy.
- Gràcia-Condal, A., Stern-Taulats, E., Planes, A., Vives, E., Mañosa, L., 2018. The giant elastocaloric effect in a Cu–Zn–Al shape-memory alloy: a calorimetric study. *Phys. Status Solidi B* 255, 1700422. <https://doi.org/10.1002/pssb.201700422>.
- Hess, T., Maier, L.M., Bachmann, N., Corhan, P., Schäfer-Welsen, O., Wöllenstein, J., Bartholomé, K., 2020. Thermal hysteresis and its impact on the efficiency of first-order caloric materials. *J. Appl. Phys.* 127, 75103. <https://doi.org/10.1063/1.5132897>.
- Hess, T., Vogel, C., Maier, L.M., Barcza, A., Vieyra, H.P., Schäfer-Welsen, O., Wöllenstein, J., Bartholomé, K., 2019. Phenomenological model for a first-order magnetocaloric material. *Int. J. Refrig.* <https://doi.org/10.1016/j.jirefrig.2019.10.003>.
- Kirsch, S.-M., Welsch, F., Michaelis, N., Schmidt, M., Wiecek, A., Frenzel, J., Eggeler, G., Schütze, A., Seelecke, S., 2018. NiTi-based elastocaloric cooling on the macroscale: from basic concepts to realization. *Energy Technol* 6, 1567–1587. <https://doi.org/10.1002/ente.201800152>.
- Kitanovski, A., Tušek, J., Tomc, U., Plaznik, U., Ozbolt, M., Poredoš, A., 2015. *Magnetocaloric Energy Conversion: From Theory to Applications*. Springer International Publishing, Cham s.l.
- Lagoudas, D.C., 2008. *Shape Memory Alloys: Modeling and Engineering Applications*. Springer Boston, MA, p. 446.
- Liang, C., Rogers, C.A., 1990. One-dimensional thermomechanical constitutive relations for shape memory materials. *J. Intell. Mater. Syst. Struct.* 1, 207–234. <https://doi.org/10.1177/1045389X9000100205>.
- Mañosa, L., Jarque-Farnos, S., Vives, E., Planes, A., 2013. Large temperature span and giant refrigerant capacity in elastocaloric Cu–Zn–Al shape memory alloys. *Appl. Phys. Lett.* 103, 211904. <https://doi.org/10.1063/1.4832339>.
- Masche, M., Ianniciello, L., Tušek, J., Engelbrecht, K., 2020. Impact of hysteresis on caloric cooling performance. *Int. J. Refrig.* <https://doi.org/10.1016/j.jirefrig.2020.10.012>.
- Ossmer, H., Lambrecht, F., Gültig, M., Chluba, C., Quandt, E., Kohl, M., 2014. Evolution of temperature profiles in TiNi films for elastocaloric cooling. *Acta Mater.* 81, 9–20. <https://doi.org/10.1016/j.actamat.2014.08.006>.
- Pataky, G.J., Ertekin, E., Sehitoglu, H., 2015. Elastocaloric cooling potential of NiTi, Ni₂FeGa, and CoNiAl. *Acta Mater.* 96, 420–427. <https://doi.org/10.1016/j.actamat.2015.06.011>.
- Porenta, L., Kabirifar, P., Žerovnik, A., Čebon, M., Žužek, B., Dolenc, M., Brojan, M., Tušek, J., 2020. Thin-walled Ni–Ti tubes under compression: ideal candidates for efficient and fatigue-resistant elastocaloric cooling. *Appl. Mater. Today* 20, 100712. <https://doi.org/10.1016/j.apmt.2020.100712>.
- Qian, S., Geng, Y., Wang, Y., Ling, J., Hwang, Y., Radermacher, R., Takeuchi, I., Cui, J., 2016. A review of elastocaloric cooling: materials, cycles and system integrations. *Int. J. Refrig.* 64, 1–19. <https://doi.org/10.1016/j.jirefrig.2015.12.001>.

- Qian, S., Ling, J., Muehlbauer, J., Hwang, Y., Radermacher, R., 2015. Study on high efficient heat recovery cycle for solid-state cooling. *Int. J. Refrig.* 55, 102–119. <https://doi.org/10.1016/j.ijrefrig.2015.03.023>.
- Smith, A., Bahl, C.R., Bjørk, R., Engelbrecht, K., Nielsen, K.K., Pryds, N., 2012. Materials challenges for high performance magnetocaloric refrigeration devices. *Adv. Energy Mater.* 2, 1288–1318. <https://doi.org/10.1002/aenm.201200167>.
- Snodgrass, R., Erickson, D., 2019. A multistage elastocaloric refrigerator and heat pump with 28 K temperature span. *Scientific reports* 9, 18532. <https://doi.org/10.1038/s41598-019-54411-8>.
- Tanaka, K., 1986. A thermomechanical sketch of shape memory effect: one-dimensional tensile behavior. *Res. Mechanica* 1986, 251–263.
- Tanaka, K., Nishimura, F., Hayashi, T., Tobushi, H., Lexcellent, C., 1995. Phenomenological analysis on subloops and cyclic behavior in shape memory alloys under mechanical and/or thermal loads. *Mech. Mater.* 19, 281–292. [https://doi.org/10.1016/0167-6636\(94\)00038-1](https://doi.org/10.1016/0167-6636(94)00038-1).
- Tušek, J., Engelbrecht, K., Mañosa, L., Vives, E., Pryds, N., 2016. Understanding the thermodynamic properties of the elastocaloric effect through experimentation and modelling. *Shap. Mem. Superelasticity* 2, 317–329. <https://doi.org/10.1007/s40830-016-0094-8>.
- Tušek, J., Engelbrecht, K., Millan-Solsona, R., Manosa, L., Vives, E., Mikkelsen, L.P., Pryds, N., 2015. The elastocaloric effect: a way to cool efficiently. *Adv. Energy Mater.* 5, 1500361 <https://doi.org/10.1002/aenm.201500361>.
- Xiao, F., Fukuda, T., Kakeshita, T., 2013. Significant elastocaloric effect in a Fe-31.2Pd (at.%) single crystal. *Appl. Phys. Lett.* 102, 161914 <https://doi.org/10.1063/1.4803168>.